electronics

MDPI

Article

Multi−Functional Gradient Fibrous Membranes Aiming at High Performance for Both Lithium–Sulfur and Zinc–Air Batteries

Congli Zhang [1], Zeyu Geng [1,2,*], Ting Meng [1,2], Fei Ma [1,2], Xueya Xu [1,2], Yang Liu [1,2] and Haifeng Zhang [1,2,*]

[1] Key Laboratory of Flexible Electronics of Zhejiang Provience, Ningbo Institute of Northwestern Polytechnical University, 218 Qingyi Road, Ningbo 315103, China
[2] Institute of Flexible Electronics, Xi'an Key Laboratory of Flexible Electronics, Northwestern Polytechnical University, Xi'an 710072, China
* Correspondence: 13914429523@mail.nwpu.edu.cn (Z.G.); iamhfzhang@nwpu.edu.cn (H.Z.); Tel.: +86-139-1442-9523 (Z.G.); +86-185-0160-0040 (H.Z.)

Abstract: Lithium–sulfur batteries have been considered one of the most promising energy storage batteries in the future of flexible and wearable electronics. However, the shuttling of polysulfides, low sulfur utilization, and bad cycle stability restricted the widespread application of lithium–sulfur batteries. Currently, gradient materials with multiple functions can solve those defects simultaneously and can be applied to various parts of batteries. Herein, an electrospinningtriple−gradient Co−N−C/PVDF/PAN fibrous membrane was prepared and applied to lithium–sulfur batteries. The Co−N−C fibrous membrane provided efficient active sites, excellent electrode conductivity, and boosted polysulfide confinement. At the same time, the PVDF/PAN membrane enhances electron transfer and lithium−ion diffusion. As a result, the integrated S@Co−N−C/PVDF/PAN/Li battery delivered a high initial capacity of 1124.1 mA h g^{-1}. Even under high sulfur loading (6 mg cm^{-2}), this flexible Li–S battery still exhibits high areal capacity (846.9 mA h cm^{-2}) without apparent capacity attenuation and security issues. Meanwhile, the gradient fibrous membranes can be used in zinc–air batteries, and the same double−gradient Co−N−C/PVDF membranes were also used as a binder−free air cathode with bifunctional catalytic activity and a facile hydrophobic and aerophile membrane, delivering remarkable cycling stability and small voltage gap in aqueous ZABs. The well−tunable structures and materials of the gradient strategy would bring inspiration for excellent performance in flexible and wearable energy storage devices.

Keywords: multi−function; gradient fibrous structure; integrated electrode; Li–S batteries; Zn–air batteries

Citation: Zhang, C.; Geng, Z.; Meng, T.; Ma, F.; Xu, X.; Liu, Y.; Zhang, H. Multi−Functional Gradient Fibrous Membranes Aiming at High Performance for Both Lithium–Sulfur and Zinc–Air Batteries. *Electronics* **2023**, *12*, 885. https://doi.org/10.3390/electronics12040885

Academic Editor: Noel Rodriguez

Received: 5 January 2023
Revised: 20 January 2023
Accepted: 6 February 2023
Published: 9 February 2023

1. Introduction

As a high theoretical specific capacity (1675 mA h g^{-1}) and low−cost battery, the lithium–sulfur battery is expected to become our next generation of energy storage devices [1–3]. However, lithium–sulfur batteries currently face many defects and problems. On the cathode side, the poor electronic conductivity of sulfur and discharged product lithium polysulfide greatly retards electron transfer upon the charge/discharge process [4]. In addition, the lithium polysulfide (LiPS) intermediates could dissolve in organic electrolytes and migrate to the anode, resulting in fast capacity decay and an inferior lifespan. Moreover, the volume expansion of long−chain lithium polysulfide ordinarily destroys the cathode material's microstructure, leading to capacity attenuation [5,6]. At the same time, the growth of lithium dendrites at the anode side can lead to the penetration of the microstructure, which causes a safety problem [7–9].

In order to solve these problems, more and more studies have started from the microstructure of anode and cathode materials, improving the conductivity of electrodes

and inhibiting the shuttle effect of polysulfide through modification aiming to improve the electrochemical stability of lithium–sulfur batteries [10–14]. In recent years, the emergence of additive manufacturing technology represented by electrospinning [15–17] and three−dimensional porous materials represented by the metal–organic framework [18–22] has triggered a new round of exploration of electrode materials. On the cathode side, electrospinning fibrous membranes can realize a simple and low−cost method to prepare stable fibrous skeletons and achieve high specific surface area and substantial active sites [23–27]. In lithium–sulfur batteries, the fibrous N−doped carbon skeleton membrane's high specific surface area and large number of high catalytic active sites can inhibit the polysulfide shuttle, resulting in better reaction kinetics and electrochemical stability [28–31]. Moreover, the fibrous N−doped carbon skeleton membrane applied in the air cathode of an aqueous zinc–air battery can also provide high functional catalytic activity in the reaction kinetics without extra adhesives/additives [32–34]. In addition, the electrospun fibrous membrane can also be used in the battery separator after simple modification [35,36]. The ultra−thin thickness of the separator can effectively reduce the ion transport distance. In Li−ion batteries, electrospun PAN and PVDF fibrous membranes soaked with electrolytes can improve the interface due to excellent mechanical properties and thermal stability [37,38]. In zinc–air batteries, the electrospun PVDF fibrous membranes can also be used as a hydrophobic and aerophilic layer replacing the expensive commercial separator [39–43]. Therefore, the advantages of composite flexible electrospinning membranes with integrated design concepts have the potential to be applied in different kinds of high−performance batteries. However, these strategies can only solve one side of battery components without an integrated solution of a full battery.

Herein, the gradient fibrous membranes were synchronously applied in lithium–sulfur and zinc–air batteries. The triple−gradient fibrous membranes not only functioned as cathode collectors (Co−N−C) but also as separators (PVDF/PAN). The bottom−layer (Co−N−C fibrous membrane can absorb polysulfide and load large amounts of sulfur. At the same time, the middle−layer PVDF/PAN provides low−tortuosity pathways for ionic transport and inhibits the shuttle effect of polysulfide coordinated with the Co−N−C layer. In addition, the triple−gradient fibrous membranes increased the flexibility of the full battery. Due to the advantages of three gradient layers, the prepared full battery showed excellent electrochemical performance, especially the capacity and cycle stability of the battery. Moreover, the multiple functions of the gradient layers endow the S@Co−N−C/PVDF/PAN/Li full battery delivering high initial capacity and excellent cycle stability even under high sulfur loading with ultra−thickness and ideal flexibility. At the same time, double−gradient Co−N−C/PVDF membranes were also successfully used as binder−free air cathodes with a high power density and superior durability for the aqueous zinc–air battery, bringing the advantage of being lighter and thinner. This work may offer a potential facile concept in fabricating flexible electrodes to achieve high performance for energy storage devices and beyond.

2. Design of Gradient Fibrous Membranes

The synchronous application of electrospinning gradient fibrous membranes in both full lithium–sulfur and zinc–air battery systems is illustrated in Figure 1a. Remarkably, the electrospinning gradient fibrous membranes can provide dual−functional applications in flexible lithium–sulfur and aqueous zinc–air batteries. The bottom−layer Co−N−C fibrous membrane has considerable potential in accelerating the kinetics of oxidation−reduction and improving active species utilization in rechargeable batteries due to the highly substantial specific surface area and surface characteristics of the Co metal. Furthermore, the top−layer PVDF/PAN fibrous membrane can serve as the insulation layer on the cathode side, restraining LiPS shuttling without affecting the transport of ions teaming up with Co−N−C when applied in a lithium–sulfur battery.

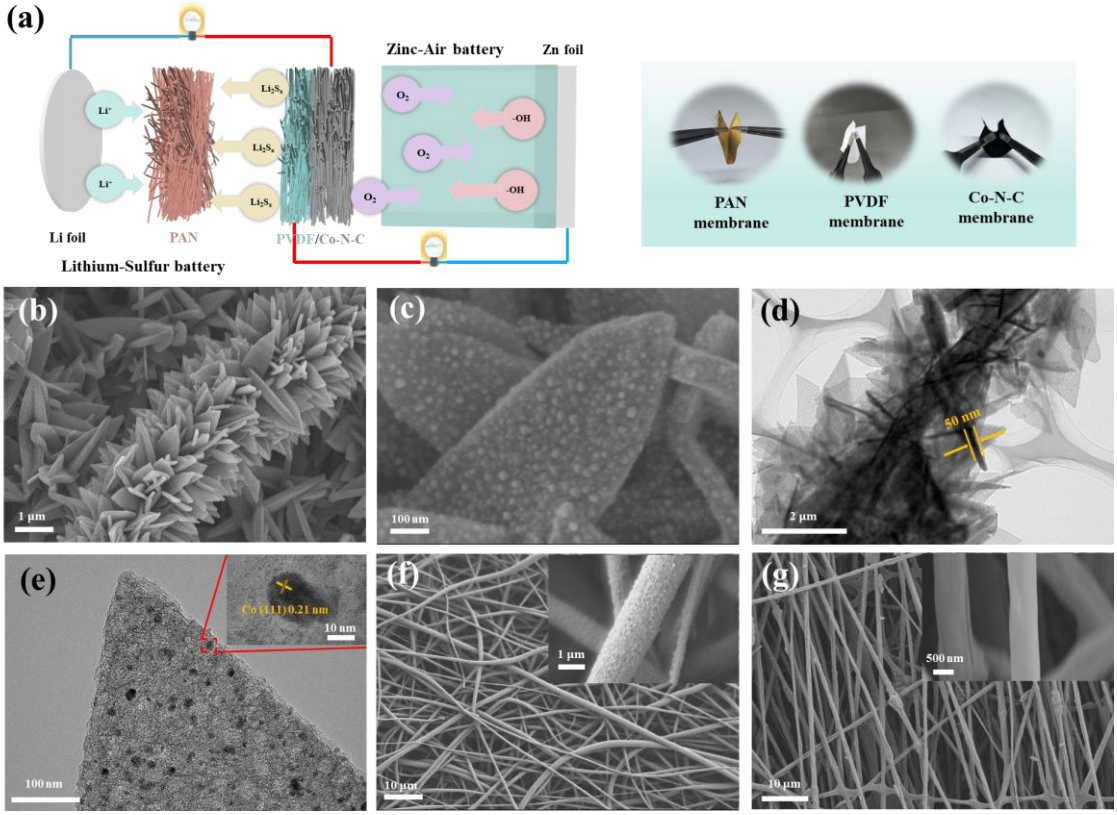

Figure 1. (**a**) Gradient flexible a lithium–sulfur battery and zinc–air battery system. Morphology characterization of Co−N−C nanosheets. (**b**,**c**) SEM images of Co−N−C. (**d**,**e**) TEM images of Co−N−C, inset: HRTEM image in the marked zone; SEM images of (**f**) PVDF fibers. (**g**) PAN fibers.

Apparently, all electrospun material had excellent flexibility and could be folded nearly up to 180°. First and foremost, PAN/Co fibrous membranes were prepared by electrospinning PAN polymer, $Co(NO_3)_2$, and MWCNTs precursor solution. In particular, the addition of MWCNTs not only increased the conductivity but also enhanced the flexibility and mechanical strength of porous cathode material. From the microscopic point of view, the prepared PAN/Co fibrous membrane had good fiber dispersion (Figure S1), and the diameter of a single fiber is about 800 nm, which is beneficial for promoting the growth of metal–organic framework (MOF) nanoparticles due to its vast specific surface area. Afterward, the PAN/Co fibrous membrane was immersed in a dimethylimidazole solution containing cobalt ions to grow flake−like Co−MOF on the fibers' surface, sufficiently obtaining PAN/Co−MOF (Figure S2). After the annealing and etching process, the organic matter on the membrane was removed, and the isolated single−atom Co was left on the fibers' surface uniformly, finally forming the Co−modified N−C skeleton membrane (Co−N−C). From SEM images, the fibrous skeleton structure coated with flake−like nanosheets remained stable after annealing at a relatively high temperature (Figure 1b) and had an extremely high specific surface area and abundant active sites (Figure 1c). Transmission electron microscopy (TEM) observations further verified the presence of the Co−modified N−C skeleton membrane (Figure 1d,e). Apparently, Co−N−C fiber presented a binary hierarchical architecture that hybridizes the fibrous skeleton (diameter about 2 μm) and in situ grown flake−like nanosheet secondary structure (length 505 nm and thickness 50 nm). Similarly, the contract sample of N−C fibrous skeleton membranes was obtained by annealing the PAN/Zn−MOF membrane, and the smooth surface was destroyed after annealing (Figure S3). These fibrous skeleton membranes were also used as the carrier of the cathode material. In addition, the representative TEM and the corresponding energy−dispersive spectroscopy (EDS) results showed that N, C, and Co elements are homogeneously distributed over the hierarchical carbon matrix. The Co

contents in the Co−N−C were about 7.47% (Figures S4 and S5). Moreover, PVDF and PAN fibrous membranes were also prepared by electrospinning technology. From SEM images (Figure 1f), the PVDF fibrous membrane had uniform dispersion and a suitable fiber diameter (about 1.5 μm). Moreover, the PAN fibrous membranes had a similar fiber dispersion, as shown in Figure 1g. The diameter of a single PAN fiber was about 600 nm. When these electrospun fibrous membranes were integrated, the gradient of material and structure (diameter: 3 μm, 1.5 μm, and 600 nm) can provide a coordination function in both lithium–sulfur and zinc–air batteries.

3. Characterization and Theoretical Simulation of Materials

X−ray diffraction (XRD) patterns of two samples were collected (Figure 2a), both of which exhibit a broad peak located at 26.2°, corresponding to the (002) plane of graphitic carbon. Significantly, the peak of 44.3° in Co−N−C confirmed the existence of the Co metal phase. The highly crystallized metallic Co nanoparticles enhanced the graphitization process of Co−N−C to a greater extent in the annealing process, improving the electrical conductivity of this fibrous membrane. Raman spectra are shown in Figure 2b. A peak located at 665 cm^{-1} in Co−N−C could further confirm metallic Co's existence, whereas it was absent in the sample of N−C. At the same time, there were two conspicuous peaks with the D band for defect carbon at 1338 cm^{-1} and the G band for graphitic carbon at 1577 cm^{-1}, respectively. The I_D/I_G ratio of Co−N−C was calculated to be 1.009, which was smaller than that of N−C (1.032), indicating an improved electron conductivity, which is beneficial for promoting charge transfer and corrosion resistance in the electrochemical process. The full X−ray photoelectron spectroscopy (XPS) spectrum showed the presence of C, N, and Co in Co−N−C and was consistent with the results of previous elemental mapping (Figure 2c and S6). The N and Co contents in Co−N−C were determined to be 7.31 at% (10.38 at% in N−C) and 7.47 at%, respectively. Both the N−doping content and extra added Co nanoparticles could effectively improve the conductivity and electrochemical activity of the original carbon electrode. The surface affinity between Co−N−C and polysulfide was tested through static adsorption tests (Figure S7) by adding an equivalent mass of Co−N−C and N−C into a 3 mL Li_2S_6 solution (6×10^{-4} M in sulfur), respectively. After soaking for 24 h, the solution exposed to Co−N−C showed lighter color and lowered ultraviolet–visible (UV–vis) absorbance than that containing N−C or pure Li_2S_6 solution without additives, indicating that Co−N−C fibrous membranes have a stronger adsorption capacity for Li_2S_6 due to their larger surface area and abundant active sites. The Co metals in Co−N−C fibrous membranes played an essential role in the chemical adsorption and catalytic conversion of polysulfide.

To further explore the excellent catalytic activity and stronger absorption of LiPSs of Co−N−C compared with N−C, density functional theory (DFT) calculations were performed. The built−up models used in the DFT calculations and their optimized adsorption configurations of the Li atoms are exhibited in Figure 2e and S8. The calculated absorption energy diagrams of the liquid–solid reaction from Li_2S_6 to Li_2S are shown in Figure 2f. The transformation from Li_2S_6 to Li_2S is regarded as the rate−limiting step in the discharging process. In the case of the Co−N−C functional fibrous skeleton, the lower Gibbs free energy of the rate−limiting step indicated the function of Co metals and the N−C skeleton, effectively lowering the energy barrier of Li_2S_6 to Li_2S conversion reaction [44].

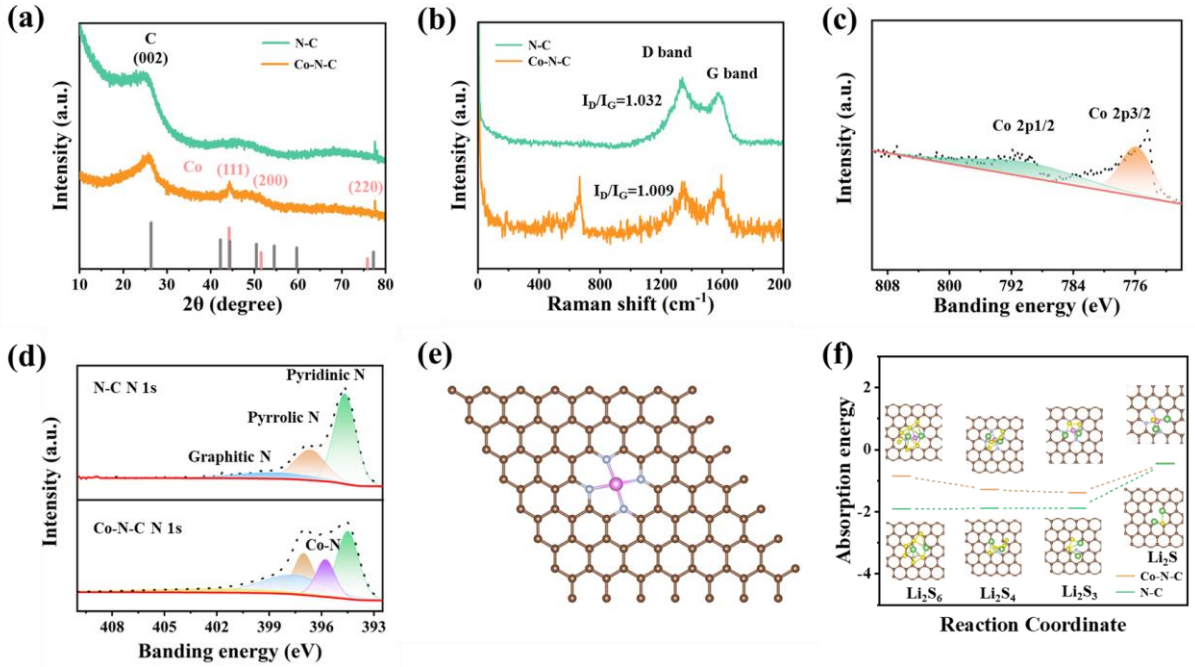

Figure 2. Structural characterization (**a**) XRD patterns of Co−N−C and N−C membrane. (**b**) Raman spectra of Co−N−C and N−C membrane. (**c**,**d**) High−resolution XPS spectra of N 1s and Co 2p for Co−N−C and N−C membrane. (**e**) The optimized configurations of Co−N−C. (**f**) Density functional theory (DFT) calculation of absorption energy between Co−N−C/N−C and $Li_2S_6/Li_2S_4/Li_2S_2/Li_2S$.

4. Electrochemical Test of Battery

4.1. Test of Li−S Battery

To demonstrate the advantages of the triple−gradient fibrous membrane in inhibiting polysulfide shuttle and enhancing the electrochemical performance, the full lithium–sulfur battery was assembled equipped with a S@Co−N−C cathode, PVDF/PAN separators, and Li foil anode. At the same time, S@N−C/PVDF/PAN/Li batteries and S@Co−N−C/PAN/Li batteries without triple gradients were assembled for comparison. Electrochemical impedance spectroscopy (EIS) measurements were first carried out to study the reaction kinetics of the fibrous skeleton. Figure 3a displays the electrochemical impedance spectra (EIS) of three kinds of membranes at open−circuit voltage. A fitted equivalent electrical circuit model is shown in Figure S9. Their Nyquist plots consisted of high−frequency semicircles and low−frequency sloped lines corresponding to the charge−transfer resistance (Rct) and mass−diffusion process, respectively [45]. At a sulfur load of 2 mg cm^{-2}, the R_{ct} value of the S@Co−N−C/PVDF/PAN/Li battery (17 Ω) was significantly lower than that of the S@Co−N−C/PAN/Li battery (47 Ω) and S@N−C/PVDF/PAN/Li battery (94 Ω). The above results demonstrated that more gradient layers could not affect faradic reaction kinetics and the ability to promote charge transfer, mainly benefiting from the improved electrical conductivity of the Co−N−C fibrous membrane and the ultra−thickness of the PVDF membrane. Furthermore, the CV plots of S@Co−N−C/PVDF/PAN/Li, S@N−C/PVDF/PAN/Li, and S@Co−N−C/PAN/Li batteries for the initial cycle were shown in Figure 3b. In comparison with S@N−C/PVDF/PAN/Li and S@Co−N−C/PAN/Li batteries, an obvious upshift of two cathodic peaks and a downshift of one anodic peak can be observed for the S@Co−N−C/PVDF/PAN/Li battery, reflecting lower polarization and faster reaction kinetics. Moreover, the two cathodic peaks at ≈2.25 V (Peak A) and ≈1.95 V (Peak B) can be ascribed to the reduction of elemental sulfur (S_8) to long−chain LiPSs and the formation of short−chain Li_2S_6/Li_2S. The broad anodic peak located at ≈2.42 V (Peak C), consisting of two overlapping anodic peaks, corresponds to the reversible transition from Li_2S_6/Li_2S to LiPSs and S_8. In this lithium–sulfur battery, the PVDF/PAN fibrous sepa-

rator had an essential influence on the reduction process from S_8 to Li_2S_x. In addition, the fibrous skeleton structure ensured that sufficient lithium−ion passed through and reacted with S_8, thus accelerating the kinetics reaction. Galvanostatic charge/discharge curves of the S@Co−N−C/PVDF/PAN/Li battery and the other two kinds of batteries were shown in Figure 3c. Two discharge and one charge characteristic voltage plateaus were observed, in keeping with the CV plots showing the lower polarization (229 mV) of the S@Co−N−C/PVDF/PAN/Li battery compared with the other two kinds of batteries, indicating the better reaction kinetics due to the higher conductivity and better catalytic ability of Co−N−C layer as well as the improvement of PVDF/PAN fibrous membranes.

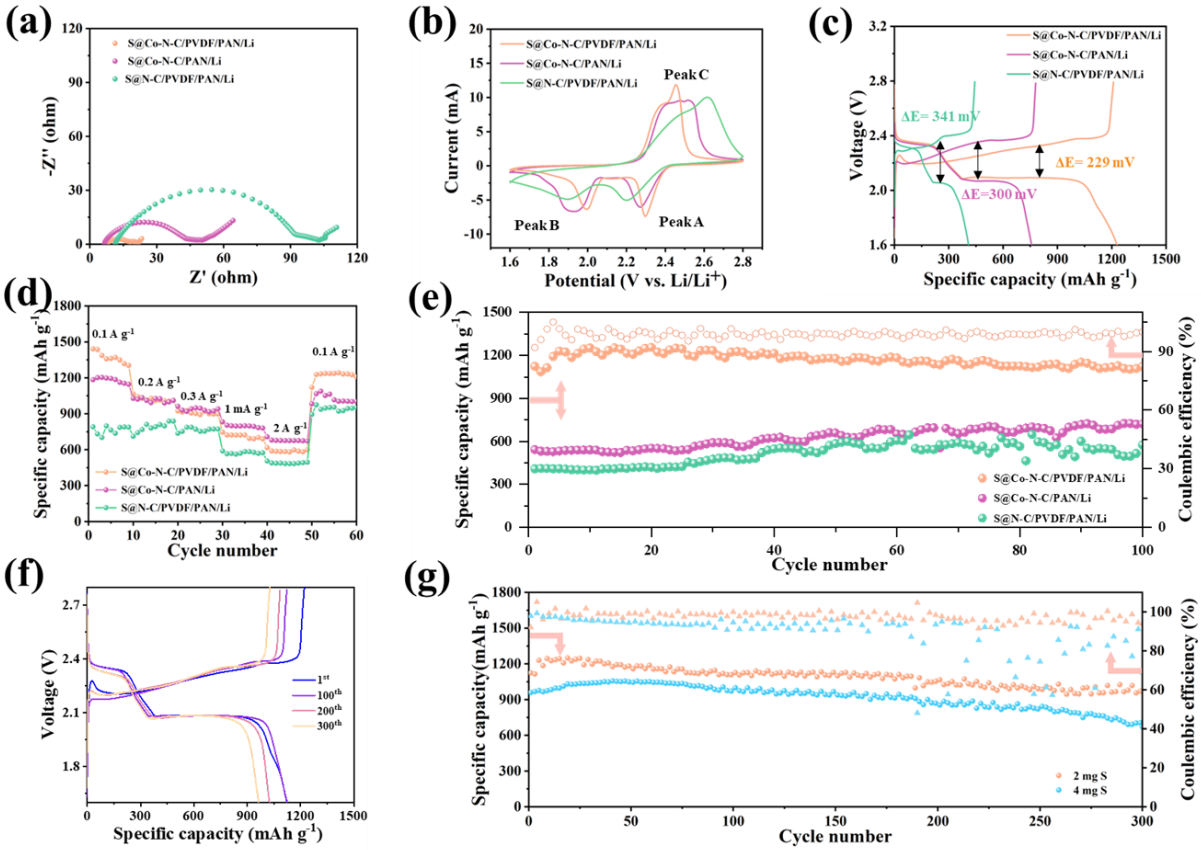

Figure 3. Electrochemical performance of S@Co−N−C/PVDF/PAN/Li, S@Co−N−C/PAN/Li, and S@N−C/PVDF/PAN/Li full batteries. (**a**) EIS curves. (**b**) CV curves. (**c**) Galvanostatic charge and discharge curves; (**d**) Rate performance from 0.15 A g^{-1} to 3 A g^{-1}. (**e**) Long−term cycling performance at 1 A g^{-1}. (**f**) Galvanostatic charge/discharge profile and cycling performance of the S@Co−N−C/PVDF/PAN/Li battery under 2 mg cm^{-2} sulfur loading at 0.5 mA cm^{-2}. (**g**) Cycling performance of the S@Co−N−C/PVDF/PAN/Li with an increased sulfur loading at 0.5 mA cm^{-2}.

Rate performance and cycling stability are also essential for the application of batteries. According to the test of rate performance (Figure 3d), the average discharge capabilities of the S@Co−N−C/PVDF/PAN/Li battery at 0.1, 0.2, 0.3, 1, and 2 A g^{-1} were 1369.4, 1018.0, 905.9, 709.7, and 588.0 mA h g^{-1}, respectively. When the current density decreased to 0.1 A g^{-1}, a high specific capacity of 1230.9 mA h g^{-1} was recovered. Compared with the other two kinds of batteries, the S@Co−N−C/PVDF/PAN/Li battery illustrated better rate performance due to its fast lithium−ion transfer and stronger polysulfide shuttling by triple−gradient Co−N−C/PVDF/PAN fibrous membranes. Moreover, the cycling stability of three kinds of batteries was tested. As shown in Figure 3e, at a current density of 0.5 A g^{-1}, the advantages of the S@Co−N−C/PVDF/PAN/Li battery in cycling stability were illustrated. This battery exhibited a high initial discharge capacity of 1124 mA h g^{-1} and maintained a high capacity of 1123 mA h g^{-1} after 100 cycles with an extremely low fad-

ing rate. It also yielded a stabilized coulombic efficiency above 99.95%, which corresponded to a slow capacity attenuation rate of remarkably. In contrast, the S@Co−N−C/PAN/Li and S@N−C/PVDF/PAN/Li batteries exhibited a relatively low initial discharge capacity of 542 and 408 mA h g^{-1} at the same current density. After about 100 cycles, the capacity was 716 and 570 mA h g^{-1}. The increased specific capacity was attributed to the slow redox kinetics and activation process. This unnormal rise of specific capacity led to the short cycling performance and sudden failure of the battery. On the contrary, the high initial capacity, high coulombic efficiency, and remarkable cycling stability demonstrated the robust coordination of the triple−gradient fibrous membrane. The effect can be reflected by the fast lithium−ion transfer in PVDF/PAN separator during the sulfur redox process. In addition, due to the existence of single−atom Co, the S@Co−N−C fibrous cathode had a high absorbing capability and strong chemical binding, restraining the polysulfide shuttling and enhancing the cycling stability of the full battery. Overall, these remarkable performances can attribute to the multiple functions of integrated fibrous membranes. At the same time, the galvanostatic charge/discharge curves of S@Co−N−C/PVDF/PAN/Li battery at different cycles (1, 50, 100, 200, and 300th) are shown in Figure 3f. Apparently, with the increase of cycle numbers, polarization had not become significantly worse (polarization was about 302 mV), indicating that reaction kinetics and reaction kinetics were not affected obviously with the increase in cycle numbers, showing the excellent performance of triple−gradient fibrous membranes.

High areal loading of sulfur is also critical for commercially high energy density lithium–sulfur batteries [46]. The long cycle performance of the S@Co−N−C/PVDF/PAN/Li battery with increased sulfur loading was tested further. The fibrous membrane of the cathode material (Co−N−C) enabled the increased sulfur loadings from 2 to 4, up to 6 mg cm^{-2} by simply adding the number of layers of the cathode material. Figure S10a displays the electrochemical impedance spectra (EIS) of the S@Co−N−C/PVDF/PAN/Li battery with increased sulfur loading. With the increased sulfur loading, the R_{ct} value remained stable without huge changes due to the adequate infiltration of electrolytes. However, the effect of interface impedance was restrained after adding Li_2S_6 solution and electrolytes, demonstrating that more fibrous membranes cannot affect faradic reaction kinetics and the ability to promote charge transfer. It mainly benefited from the improved electrical conductivity of the Co−N−C fibrous membrane and the ultra−thickness of PVDF fibrous. Galvanostatic charge/discharge curves are shown in Figure S10b. Two discharge and one charge characteristic voltage plateaus were still observed, showing a stable polarization of about 352 mV and 380 mV with the increase of the sulfur loading, indicating better reaction kinetics without the effect of mass polysulfide. Moreover, the long cycling performance is shown in Figure 3g. When the number of cycles reaches 300, the capacity of the S@Co−N−C/PVDF/PAN/Li battery remained at 965 mA h g^{-1} under a load of 2 mg S load at 0.5 A g^{-1}. At the same time, under a load of 4 mg S load at 0.5 A g^{-1}, the battery remained at an ideal capacity of 705 mA h g^{-1} with a low fading rate of 0.088% per cycle after over 300 cycles. Notably, even at an ultrahigh sulfur loading of 6 mg cm^{-2} (Figure S10c), this battery equipped with a multi−layer integrated fibrous membrane still exhibited a high initial specific capacity of 846 mA h g^{-1}. After 60 cycles, the capacity was about 962 mA h g^{-1}, proving that the integrated membranes were beneficial to sulfur redox utilization and kinetics. These performances confirmed the advantages of gradient electrospinning fibrous membranes,(Table S1) again laying a solid foundation for the commercial application of lithium–sulfur batteries [47–54].

To better reflect the coordinating advantage of triple−gradient Co−N−C/PVDF/PAN fibrous membranes in lithium–sulfur batteries, post−characterizations were conducted. The S@Co−N−C/PVDF/PAN/Li battery was disassembled. The Co−N−C, PVDF, and PAN membranes were taken out, and we conducted ex situ observation. Figure S11 illustrates SEM images of three fibrous membranes (Co−N−C, PVDF, PAN) after over 100 charge/discharge cycles. As for the Co−N−C fibrous membrane (Figure S11a), the flake−like fibrous skeleton remained intact and continuous throughout cycling, demon-

strating the remarkable electrochemical stability of this material. It is apparent that the fiber diameter had an apparent increase; meanwhile, the surface of the fibers was covered with thick sulfur−containing deposits. This proved the ability to restrain the polysulfide shuttling and adsorption properties of the Co−N−C fibrous membranes during cycling. The adhesive reticular morphology in Figure S11b,c was due to the high electrolyte uptake and powerful polysulfide absorption of PVDF/PAN fibrous membranes. This effect can be attributed to the electrospun triple−gradient fibrous membranes applied in the separator, reflecting the potential of restraining the shuttle effect.

4.2. Test of ORR and OER

It is worth noting that due to the excellent adsorption properties of gradient fibrous membranes, we also explored the possibility of applying the Co−N−C/PVDF membrane structure as a double gradient to the zinc–air battery. Before the application of gradient Co−N−C/PVDF fibrous membranes in zinc–air batteries, the electrocatalytic activity was explored. The ORR catalytic performance of Co−N−C and N−C was evaluated in a 0.1 M KOH electrolyte by a rotating−ring disk electrode. Cyclic voltammogram (CV) curves of Co−N−C and N−C showed a distinct ORR peak in the O_2_saturated solution compared with that in the N_2_saturated electrolyte (Figure 4a and Figure S12a). The ORR linear sweep voltammetry (LSV) polarization curves in a rotational rate of 1600 rpm (Figure 4b and S12b) showed that Co−N−C possessed a higher ORR half−wave potential ($E_{1/2}$) of 0.74 V, more positive than those of N−C ($E_{1/2}$ = 0.63 V). Meanwhile, Co−N−C illustrated a lower Tafel slope of 65.49 mV dec^{-1} compared with the figure of N−C (75.47 mV dec^{-1}), suggesting faster ORR kinetics (Figure 4c). Specifically, the Co−N−C exhibited a high current density (j_d) of 4.082 mA cm^{-2} at 0.20 V, which was higher than that of N−C (3.811 mA cm^{-2} at 0.20 V), as shown in Figure S13. The corresponding Koutecky–Levich plots are shown in Figure 4b and Figure S12b insert. The slope of the plots indicates the electron transfer number (n), showing that Co−N−C involves a direct 4−electron transfer pathway towards ORR, with better catalytic activity than N−C (n = 2.9). The OER catalytic activities were tested in a 1 M KOH electrolyte by the same rotating disk electrode. As shown in the LSV polarization curves (Figure 4d), Co−N−C achieved a current density of 10 mA cm^{-2} with an overpotential of 564 mV, which is much lower than that of N−C (773 mV). In addition, the Tafel slope of 40.62 mV dec^{-1} for Co−N−C is smaller than that of N−C (57.83 mV dec^{-1}) in Figure 4e, proving better kinetics for OER. To evaluate the dual−functional catalytic activities of two different samples, the potential difference between OER (E_{j10}) and ORR ($E_{1/2}$) ($\Delta E = E_{j10} - E_{1/2}$) was calculated. As shown in Figure 4f, the reversible oxygen overpotential of Co−N−C was 0.877 V, lower than that of N−C (1.187 V). The superior activity of single Co atom sites for ORR and OER makes Co−N−C promising for next−generation Zn–air batteries.

4.3. Test of the Zn–Air Battery

To demonstrate the dual functions of double−gradient Co−N−C/PVDF fibrous membrane, we conducted tests in aqueous Zn–air batteries (ZABs). Benefiting from the double−gradient self−supporting structure obtained by electrospinning, the Co−N−C membrane can be used as a binder−free air cathode, and the PVDF membrane can be used as a hydrophobic and aerophilic layer. Initially, the measured contact angle on the electrospinning PVDF membrane was ~92° (Figure S14), indicating its excellent performance hydrophobicity that can replace the expansive commercial hydrophobic layer [55]. Intuitively, the PVDF membrane showed a thinner thickness (130 μm), almost 45% of the thickness of the commercial hydrophobic layer (360 μm), as shown in Figure S15a,b. Furthermore, the thinner thickness led to the lighter mass of the hydrophobic and aerophilic layer, as shown in Figure S15c,d. The PVDF membrane had a 56% reduction in mass per square centimeter compared to the commercial hydrophobic layer (10.8 mg and 24.2 mg, respectively). This feature laid the foundation for assembling thinner ZABs. Remarkably, the lighter weight did not affect the performance of the ZABs. After replacing the commercial

hydrophobic diaphragm, the ZABs equipped with PVDF fibrous membranes showed ideal electrochemical performance.

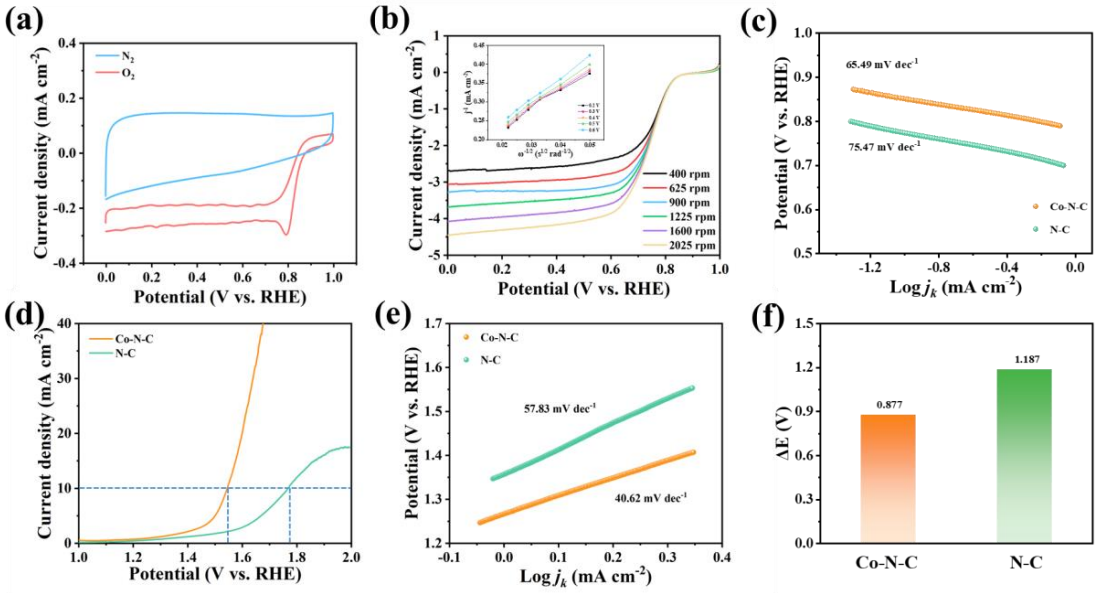

Figure 4. (**a**) CV curves of Co−N−C of ORR in the N_2−/O_2−saturated KOH (0.1 m). (**b**) LSV curves of ORR at different rotational rates (r.p.m.) and corresponding K−L plots (inset section) of Co−N−C. (**c**) Tafel plots of ORR. (**d**) OER LSV polarization curves. (**e**) Tafel plots of ORR. (**f**) The overall potential gap (ΔE) between the OER potential measured at a current density of 10 mA cm^{-2} and the ORR half−wave potential ($\Delta E = E_{j10} - E_{1/2}$).

Herein a Co−N−C fibrous membrane functioning as a cathode to promote efficient ORR/OER bifunctional oxygen electrocatalysis, a PVDF fibrous membrane serving as a hydrophobic and aerophilic layer, and a zinc plate functioning as an anode to provide a zinc source and an electrolyte (6 M KOH + 0.2 M $Zn(CH_3COO)_2$) could facilitate the diffusion of OH− and other species [56]. This battery showed a higher open−circuit voltage (OCV) of 1.38 V compared to 1.23 V for the N−C−based zinc–air battery (Figure 5a). The charge−discharge polarization curves (Figure 5b) and corresponding power density curves (Figure 5c) further revealed the potential of Co−N−C for ZABs. The peak power density of Co−N−C/PVDF was 1.81 mW cm^{-2}, which was much higher than that of N−C/PVDF (0.92 mW cm^{-2}). Moreover, the double−gradient Co−N−C/PVDF−based ZABs showed higher specific capacities when compared with N−C/PVDF−based ZABs, such as 760 mA h g_{Zn}^{-1} of Co−N−C/PVDF and 578 mA h g_{Zn}^{-1} of N−C/PVDF at 1 mA cm^{-2} (Figure 5d). Furthermore, galvanostatic cycling tests were conducted to clarify the durability of the Co−N−C/PVDF and N−C/PVDF for the aqueous ZABs. As shown in Figure 5e, the Co−N−C/PVDF−based battery initially had a remarkably smaller voltage gap (1.09 V) compared with the N−C/PVDF−based battery (1.33 V). Furthermore, the Co−N−C/PVDF−based battery illustrated cycling stability of 2500 cycles (over 250 h) at 1 mA cm^{-2}, maintaining an ideal voltage gap (0.85 V), while the value of N−C/PVDF−based ZABs was 1.54 V. The Co−N−C/PVDF−based aqueous ZAB exhibited cycling stability of 5000 cycles for 500 h at 1 mA cm^{-2} with a final voltage gap of 0.93 V, while the N−C/PVDF−based aqueous ZAB is failure after only 300 h cycling. The detailed cycling curves are shown in Figure S16. Apparently, the charge/discharge profile is stable and the voltage gap is homogeneous in any cycling stages. After the cycling test of the zinc–air battery, the Co−N−C, and N−C fibrous membranes were taken out, and SEM images were taken, as shown in Figure S17. Apparently, due to the advantages of a huge specific surface area to load active sites, the ability of Co−N−C to absorb electrolytes was stronger than N−C. On the contrary, the N−C fibrous membrane was lacking single atom

Co and high specific surface area and exhibited a lack of adsorption capacity for the electrolyte (Table S2) [57–61]. Overall, the unique double−gradient Co−N−C/PVDF−based air cathode showed an excellent performance in the application of aqueous ZABs.

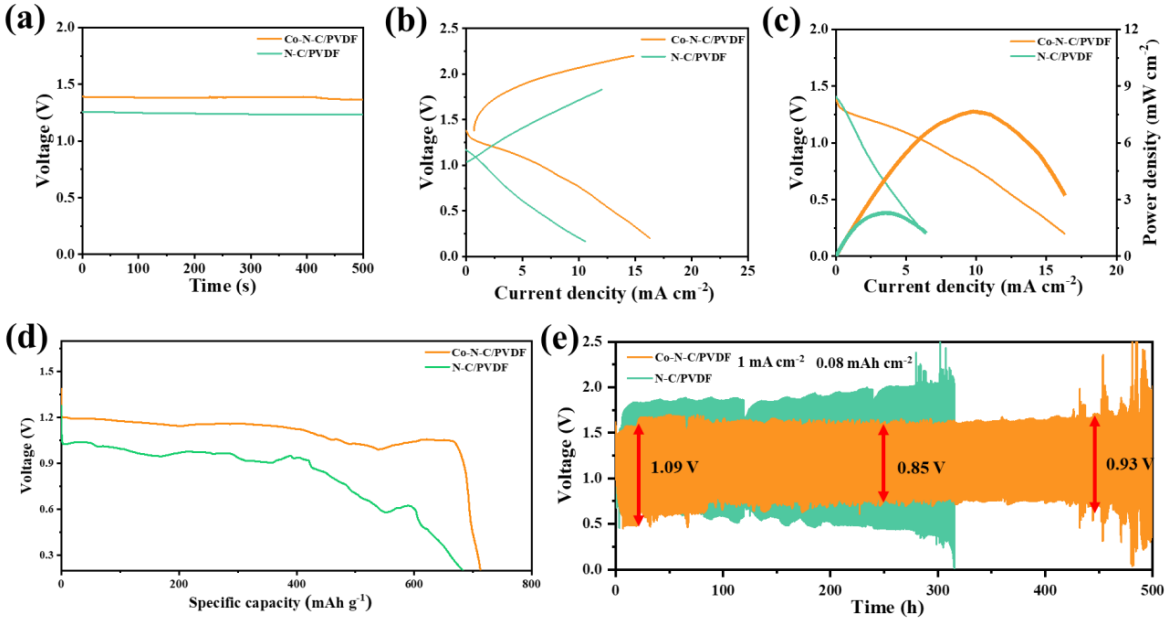

Figure 5. Electrochemical performance of Co−N−C in aqueous Zn–air battery. (**a**) Open−circuit voltage curves. (**b**) Charge−discharge polarization curves;.(**c**) Power density curves of the Co−N−C. (**d**) Zn mass−normalized specific capacities. (**e**) Galvanostatic cycling tests at 1 mA cm^{-2} for Co−N−C.

5. Conclusions

In summary, we developed gradient fibrous membranes that integrated gradient materials and structure by electrospinning technology in lithium–sulfur and zinc–air batteries. The triple−gradient design synergistically provides an enormous specific surface area, loads more active sites, and inhibits the shuttle of polysulfides. Finally, the lithium–sulfur battery showed faster reaction kinetics, better specific capacity, and cycling stability (965 mA h g^{-1} after 300 cycles at 2 mg S/0.5 A g^{-1} and 962 mA h g^{-1} after 60 cycles at 6 mg S/0.5 A g^{-1}). At the same time, the Co−N−C fibrous membranes exhibited ideal ORR/OER bifunctional oxygen electrocatalytic activity and laid a solid foundation for the application of double−gradient Co−N−C/PVDF fibrous membranes in aqueous zinc–air batteries (500 h at 1 mA cm^{-2}/0.08 mA h cm^{-2}). Consequently, the electrospun gradient fibrous membranes demonstrated remarkably high performance in both lithium–sulfur and zinc–air batteries, with the potential for the future development of flexible and wearable energy storage devices.

Supplementary Materials: The following supporting information can be downloaded at: https://www.mdpi.com/article/10.3390/electronics12040885/s1, **Figure S1.** SEM images (a) PAN/Co fibers; (d) Single PAN/Co fiber; **Figure S2.** SEM images (a) PAN/Co-MOF fibers; (d) Single Co-MOF flake; **Figure S3.** SEM images (a) PAN/Zn fibers; (b) Single PAN/Zn fiber; (c) PAN/Zn-MOF fiber; (d) Single Zn-MOF flake; (e-f) Single N-C fiber with increasing magnifications; **Figure S4.** TEM image and the corresponding elemental maps of Co-N-C; **Figure S5.** TEM image and the corresponding elemental maps of N-C; **Figure S6.** XPS (a) full spectrum and (b) high-resolution C 1s spectra for Co-N-C and N-C; **Figure S7.** UV–vis spectra and corresponding image (inset) of pure Li_2S_6 solution before and after static adsorption of Li_2S_6 by N-C and Co-N-C; **Figure S8.** (a) The optimized configurations of N-C; (b) Adsorption model of Li_2S_6/ Li_2S_4 / Li_2S_2/ Li_2S on N-C surface; **Figure S9.** Equivalent circuit model and related results for analyzing the impedance spectra shown in Figure 3a; **Figure S10.** electrochemical performance of S@Co-N-C/PVDF/PAN/Li battery with an increasing S loading. (a) EIS curves; (b) Galvanostatic charge/discharge profile of the S@Co-N-C/PVDF/PAN/Li battery with

an increasing S loading at 0.5 mA cm^{-2}; (c) Cycling performance of the S@Co-N-C/PVDF /PAN/Li of 6 mg sulfur loading at 0.5 mA cm^{-2}; **Figure S11.** SEM images of parts in S@Co-N-C/PVDF/PAN/Li battery (a) Co-N-C layer after 100 cycles; (b) PVDF layer after cycles; (c) PAN layer after cycles; **Figure S12.** Electrochemical performance of Co-N-C in ORR (a) CV curves of N-C in the N_2-/O_2-saturated KOH (0.1 m), (b) LSV curves at different rotational rates (r.p.m.) and corresponding K−L plots (inset section) of N-C; **Figure S13.** Contrast of $E_{1/2}$ and j_d of ORR; **Figure S14.** The measured surface contact angle of electrolyte on PVDF; **Figure S15.** Display of thickness and weight about two kinds of membranes (a) The thickness of PVDF layer; (b) The thickness of commercial hydrophobic layer; (c) The weights of PVDF layer per square centimeter; (d) The weights of commercial hydrophobic layer per square centimeter; **Figure S16.** detailed cycling curves for Co-N-C with different cycles from Figure 5e (a) cycles of 501-510th; (b) cycles of 2001-2010th; (c) cycles of 4001-4010th; **Figure S17.** SEM images after 1000 cycles test of aqueous Zinc-Air battery (a) Co-N-C fibers; (b) N-C fiber; **Table S1.** Performance comparison of single-atom based sulfur hosts and Li-S batteries between this work and reported studies; **Table S2.** Performance comparison of recently bifunctional electrocatalysts and aqueous ZABs prepared by electrospinning method between this work and reported studies.

Author Contributions: Conceptualization, C.Z. and Z.G.; Methodology, C.Z. and Z.G.; Validation, C.Z., Z.G. and T.M.; Formal Analysis, C.Z.; Investigation, Z.G.; Resources, T.M., F.M., X.X. and Y.L.; Writing—Original Draft Preparation, C.Z. and Z.G.; Writing—Review and Editing, C.Z.; Supervision, H.Z.; Project Administration, Z.G. and H.Z. All authors have read and agreed to the published version of the manuscript.

Funding: This work is supported by the National Natural Science Foundation of China (Grant No. 21905059 and No. 22279103), the fellowship of China Postdoctoral Science Foundation (2022M722596), the Innovation Foundation for Doctor Dissertation of Northwestern Polytechnical University (No. CX2021122).

Institutional Review Board Statement: Not applicable.

Informed Consent Statement: Not applicable.

Data Availability Statement: Not applicable.

Conflicts of Interest: The authors declare no conflict of interest.

References

1. Zhang, Q.; Li, F.; Huang, J.-Q.; Li, H. Lithium−Sulfur Batteries: Co−Existence of Challenges and Opportunities. *Adv. Funct. Mater.* **2018**, *28*, 1804589.
2. Yang, T.; Xia, J.; Piao, Z.; Yang, L.; Zhang, S.; Xing, Y.; Zhou, G. Graphene−Based Materials for Flexible Lithium−Sulfur Batteries. *ACS Nano* **2021**, *15*, 13901–13923. [CrossRef] [PubMed]
3. Huang, Z.H.; Wei, J.S.; Song, T.B.; Ni, J.W.; Wang, F.; Xiong, H.M. Carbon dots crosslinked gel polymer electrolytes for dendrite−free and long−cycle lithium metal batteries. *SmartMat* **2022**, *3*, 323–336. [CrossRef]
4. Zhang, T.; Qiu, D.; Hou, Y. Free−standing and consecutive ZnSe@carbon nanofibers architectures as ultra−long lifespan anode for flexible lithium−ion batteries. *Nano Energy* **2022**, *94*, 106909. [CrossRef]
5. Gao, C.; Jiang, Z.; Qi, S.; Wang, P.; Jensen, L.R.; Johansen, M.; Christensen, C.K.; Zhang, Y.; Ravnsbæk, D.B.; Yue, Y. Metal−organic framework glass anode with an exceptional cycling−induced capacity enhancement for lithium−ion batteries. *Adv. Mater.* **2021**, *34*, 2110048. [CrossRef]
6. Ye, Z.; Jiang, Y.; Li, L.; Wu, F.; Chen, R. Rational Design of MOF−Based Materials for Next−Generation Rechargeable Batteries. *Nano−Micro Lett.* **2021**, *13*, 203. [CrossRef]
7. Zhang, H.; Wang, L.; Li, H.; He, X. Criterion for Identifying Anodes for Practically Accessible High−Energy−Density Lithium−Ion Batteries. *ACS Energy Lett.* **2021**, *6*, 3719–3724. [CrossRef]
8. Zhao, S.; He, D.; Wu, T.; Wang, L.; Yu, H. Ultrastable Orthorhombic Na_2TiSiO_5 Anode for Lithium−Ion Battery. *Adv. Energy Mater.* **2021**, *12*, 2102709.
9. Liu, S.; Kang, L.; Henzie, J.; Zhang, J.; Ha, J.; Amin, M.A.; Hossain, M.S.A.; Jun, S.C.; Yamauchi, Y. Recent Advances and Perspectives of Battery−Type Anode Materials for Potassium Ion Storage. *ACS Nano* **2021**, *15*, 18931–18973.
10. Tong, Z.; Huang, L.; Lei, W.; Zhang, H.; Zhang, S. Carbon−containing electrospun nanofibers for lithium–sulfur battery: Current status and future directions. *J. Energy. Chem.* **2021**, *54*, 254–273.
11. Liu, Y.; Meng, X.; Wang, Z.; Qiu, J. A Li_2S−based all−solid−state battery with high energy and superior safety. *Sci. Adv.* **2022**, *8*, 8390. [CrossRef] [PubMed]
12. Zhang, H.; Ono, L.K.; Tong, G.; Liu, Y.; Qi, Y. Long−life lithium−sulfur batteries with high areal capacity based on coaxial CNTs@TiN−TiO_2 sponge. *Nat. Commun.* **2021**, *12*, 4738. [CrossRef] [PubMed]

13. Cai, J.; Song, Y.; Chen, X.; Sun, Z.; Yi, Y.; Sun, J.; Zhang, Q. MOF−derived conductive carbon nitrides for separator−modified Li–S batteries and flexible supercapacitors. *J. Mater. Chem. A* **2020**, *8*, 1757–1766.
14. Lyu, J.-Y.; Chen, S.; He, W.; Zhang, X.−X.; Tang, D.−y.; Liu, P.−J.; Yan, Q.−L. Fabrication of high−performance graphene oxide doped PVDF/CuO/Al nanocomposites via electrospinning. *Chem. Eng. J.* **2019**, *368*, 129–137. [CrossRef]
15. Wang, J.; Lin, J.; Chen, L.; Deng, L.; Cui, W. Endogenous Electric−Field−Coupled Electrospun Short Fiber via Collecting Wound Exudation. *Adv. Mater.* **2021**, *34*, 2108325.
16. Le, T.T.; Curry, E.J.; Vinikoor, T.; Das, R.; Liu, Y.; Sheets, D.; Tran, K.T.M.; Hawxhurst, C.J.; Stevens, J.F.; Hancock, J.N.; et al. Piezoelectric Nanofiber Membrane for Reusable, Stable, and Highly Functional Face Mask Filter with Long−Term Biodegradability. *Adv. Funct. Mater.* **2022**, *32*, 2113040. [CrossRef]
17. Guo, J.; Fu, S.; Deng, Y.; Xu, X.; Laima, S.; Liu, D.; Zhang, P.; Zhou, J.; Zhao, H.; Yu, H.; et al. Hypocrystalline ceramic aerogels for thermal insulation at extreme conditions. *Nature* **2022**, *606*, 909–916. [CrossRef]
18. He, Y.; Qiao, Y.; Chang, Z.; Zhou, H. The potential of electrolyte filled MOF membranes as ionic sieves in rechargeable batteries. *Energy Environ. Sci.* **2019**, *12*, 2327–2344.
19. Geng, P.; Du, M.; Guo, X.; Pang, H.; Tian, Z.; Braunstein, P.; Xu, Q. Bimetallic Metal−Organic Framework with High−Adsorption Capacity toward Lithium Polysulfides for Lithium–sulfur Batteries. *Energy Environ. Mater.* **2021**, *5*, 599–607. [CrossRef]
20. Lin, J.-B.; Nguyen, T.T.T.; Vaidhyanathan, R.; Burner, J.; Taylor, J.M.; Durekova, H.; Akhtar, F.; Mah, R.K.; Ghaffari−Nik, O.; Marx, S.; et al. A scalable metal−organic framework as a durable physisorbent for carbon dioxide capture. *Science* **2021**, *374*, 1464–1469.
21. He, Y.; Chang, Z.; Wu, S.; Qiao, Y.; Bai, S.; Jiang, K.; He, P.; Zhou, H. Simultaneously Inhibiting Lithium Dendrites Growth and Polysulfides Shuttle by a Flexible MOF−Based Membrane in Li−S Batteries. *Adv. Energy Mater.* **2018**, *8*, 1802130. [CrossRef]
22. Chen, X.; Xie, H.; Lorenzo, E.R.; Zeman, C.J.t.; Qi, Y.; Syed, Z.H.; Stone, A.; Wang, Y.; Goswami, S.; Li, P.; et al. Direct Observation of Modulated Radical Spin States in Metal−Organic Frameworks by Controlled Flexibility. *J. Am. Chem. Soc.* **2022**, *144*, 2685–2693. [PubMed]
23. Yan, Y.; Liu, X.; Yan, J.; Guan, C.; Wang, J. Electrospun Nanofibers for New Generation Flexible Energy Storage. *Energy Environ. Mater.* **2020**, *4*, 502–521.
24. Shi, S.; Si, Y.; Han, Y.; Wu, T.; Iqbal, M.I.; Fei, B.; Li, R.K.Y.; Hu, J.; Qu, J. Recent Progress in Protective Membranes Fabricated Via Electrospinning: Advanced Materials, Biomimetic Structures, and Functional Applications. *Adv. Mater.* **2021**, *34*, 2107938. [CrossRef]
25. Li, X.; Chen, W.; Qian, Q.; Huang, H.; Chen, Y.; Wang, Z.; Chen, Q.; Yang, J.; Li, J.; Mai, Y.W. Electrospinning−Based Strategies for Battery Materials. *Adv. Energy Mater.* **2020**, *11*, 2000845.
26. Lei, W.; Li, H.; Tang, Y.; Shao, H. Progress and perspectives on electrospinning techniques for solid−state lithium batteries. *Carbon Energy* **2022**, *4*, 539–575. [CrossRef]
27. Che, H.; Yuan, J. Recent advances in electrospinning supramolecular systems. *J. Mater. Chem. B* **2021**, *10*, 8–19.
28. Wang, J.; Yang, G.; Chen, J.; Liu, Y.; Wang, Y.; Lao, C.Y.; Xi, K.; Yang, D.; Harris, C.J.; Yan, W.; et al. Flexible and High−Loading Lithium–Sulfur Batteries Enabled by Integrated Three−In−One Fibrous Membranes. *Adv. Energy Mater.* **2019**, *9*, 1902001.
29. Huang, T.; Sun, Y.; Wu, J.; Jin, J.; Wei, C.; Shi, Z.; Wang, M.; Cai, J.; An, X.T.; Wang, P.; et al. A Dual−Functional Fibrous Skeleton Implanted with Single−Atomic Co−N_x Dispersions for Longevous Li−S Full Batteries. *ACS Nano* **2021**, *15*, 14105–14115.
30. Kang, L.; Zhang, M.; Zhang, J.; Liu, S.; Zhang, N.; Yao, W.; Ye, Y.; Luo, C.; Gong, Z.; Wang, C.; et al. Correction: Dual−defect surface engineering of bimetallic sulfide nanotubes towards flexible asymmetric solid−state supercapacitors. *J. Mater. Chem. A* **2020**, *8*, 25443–25444. [CrossRef]
31. Liu, S.; Yin, Y.; Shen, Y.; Hui, K.S.; Chun, Y.T.; Kim, J.M.; Hui, K.N.; Zhang, L.; Jun, S.C. Phosphorus Regulated Cobalt Oxide@Nitrogen−Doped Carbon Nanowires for Flexible Quasi−Solid−State Supercapacitors. *Small* **2020**, *16*, e1906458. [CrossRef] [PubMed]
32. Han, Y.; Duan, H.; Zhou, C.; Meng, H.; Jiang, Q.; Wang, B.; Yan, W.; Zhang, R. Stabilizing Cobalt Single Atoms via Flexible Carbon Membranes as Bifunctional Electrocatalysts for Binder−Free Zinc−Air Batteries. *Nano Lett.* **2022**, *22*, 2497–2505. [CrossRef] [PubMed]
33. Gao, K.; Shen, M.; Duan, C.; Xiong, C.; Dai, L.; Zhao, W.; Lu, W.; Ding, S.; Ni, Y. Co−N−Doped Directional Multichannel PAN/CA−Based Electrospun Carbon Nanofibers as High−Efficiency Bifunctional Oxygen Electrocatalysts for Zn–Air Batteries. *ACS Sustain. Chem. Eng.* **2021**, *9*, 17068–17077.
34. Yu, P.; Wang, L.; Sun, F.; Xie, Y.; Liu, X.; Ma, J.; Wang, X.; Tian, C.; Li, J.; Fu, H. Co Nanoislands Rooted on Co−N−C Nanosheets as Efficient Oxygen Electrocatalyst for Zn−Air Batteries. *Adv. Mater.* **2019**, *31*, 1901666.
35. Liang, Y.; Ma, D.; Zhao, N.; Wang, Y.; Yang, M.; Ruan, J.; Yang, G.; Mi, H.; He, C.; Zhang, P. Novel Concept of Separator Design: Efficient Ions Transport Modulator Enabled by Dual−Interface Engineering Toward Ultra−Stable Zn Metal Anodes. *Adv. Funct. Mater.* **2022**, *32*, 2112936. [CrossRef]
36. Liu, Q.; Wang, Y.; Hong, X.; Zhou, R.; Hou, Z.; Zhang, B. Elastomer–Alginate Interface for High−Power and High−Energy Zn Metal Anodes. *Adv. Energy Mater.* **2022**, *12*, 2200318.
37. Ma, Y.; Wan, J.; Yang, Y.; Ye, Y.; Xiao, X.; Boyle, D.T.; Burke, W.; Huang, Z.; Chen, H.; Cui, Y.; et al. Scalable, Ultrathin, and High−Temperature−Resistant Solid Polymer Electrolytes for Energy−Dense Lithium Metal Batteries. *Adv. Energy Mater.* **2022**, *12*, 2103720. [CrossRef]

38. Ryu, J.; Han, D.-Y.; Hong, D.; Park, S. A polymeric separator membrane with chemoresistance and high Li−ion flux for high−energy−density lithium metal batteries. *Energy Storage Mater.* **2021**, *45*, 941–951.
39. Liu, S.; Zhou, L.; Han, J.; Wen, K.; Guan, S.; Xue, C.; Zhang, Z.; Xu, B.; Lin, Y.; Shen, Y.; et al. Super Long−Cycling All−Solid−State Battery with Thin Li_6PS_5Cl−Based Electrolyte. *Adv. Energy Mater.* **2022**, *12*, 2200660.
40. Xia, C.; Huang, L.; Yan, D.; Douka, A.I.; Guo, W.; Qi, K.; Xia, B.Y. Electrospinning Synthesis of Self−Standing Cobalt/Nanocarbon Hybrid Membrane for Long−Life Rechargeable Zinc–Air Batteries. *Adv. Funct. Mater.* **2021**, *31*, 2105021. [CrossRef]
41. Zhou, Y.; Xie, M.; Song, Y.; Yan, D.; Wang, Z.; Zhang, S.; Deng, C. Edge−enriched Ni−N_4 atomic sites embedded enoki−mushroom−like carbon nanotubes assembling hollow fibers for CO_2 conversion and flexible Zn−air battery. *Energy Stor. Mater.* **2022**, *47*, 235–248.
42. Xu, Z.; Zhu, J.; Shao, J.; Xia, Y.; Tseng, J.; Jiao, C.; Ren, G.; Liu, P.; Li, G.; Chen, R.; et al. Atomically dispersed cobalt in core−shell carbon nanofiber membranes as super−flexible freestanding air−electrodes for wearable Zn−air batteries. *Energy Stor. Mater.* **2022**, *47*, 365–375. [CrossRef]
43. Zhang, W.; Xu, C.H.; Zheng, H.; Li, R.; Zhou, K. Oxygen−Rich Cobalt–Nitrogen–Carbon Porous Nanosheets for Bifunctional Oxygen Electrocatalysis. *Adv. Funct. Mater.* **2022**, *32*, 2200763. [CrossRef]
44. Wang, R.; Wu, R.; Yan, X.; Liu, D.; Guo, P.; Li, W.; Pan, H. Implanting Single Zn Atoms Coupled with Metallic Co Nanoparticles into Porous Carbon Nanosheets Grafted with Carbon Nanotubes for High−Performance Lithium−Sulfur Batteries. *Adv. Funct. Mater.* **2022**, *32*, 2200424. [CrossRef]
45. Yu, M.; Wang, Z.; Wang, Y.; Dong, Y.; Qiu, J. Freestanding Flexible Li_2S Paper Electrode with High Mass and Capacity Loading for High−Energy Li−S Batteries. *Adv. Energy Mater.* **2017**, *7*, 1700018. [CrossRef]
46. Du, M.; Li, Q.; Zhang, G.; Wang, F.; Pang, H. Metal–Organic Framework−Based Sulfur−Loaded Materials. *Energy Environ. Sci.* **2021**. [CrossRef]
47. Li, Y.; Wang, W.; Zhang, B.; Fu, L.; Wan, M.; Li, G.; Cai, Z.; Tu, S.; Duan, X.; Seh, Z.W.; et al. Manipulating Redox Kinetics of Sulfur Species Using Mott–Schottky Electrocatalysts for Advanced Lithium–Sulfur Batteries. *Nano Lett.* **2021**, *21*, 6656–6663.
48. Shao, Q.; Xu, L.; Guo, D.; Su, Y.; Chen, J. Atomic level design of single iron atom embedded mesoporous hollow carbon spheres as multi-effect nanoreactors for advanced lithium-sulfur batteries. *J. Mater. Chem. A* **2020**, *8*, 23772–23783.
49. Qiu, Y.; Fan, L.; Wang, M.; Yin, X.; Wu, X.; Sun, X.; Tian, D.; Guan, B.; Tang, D.; Zhang, N. Precise Synthesis of Fe-N_2 Sites with High Activity and Stability for Long-Life Lithium-Sulfur Batteries. *ACS Nano* **2020**, *14*, 16105–16113.
50. Du, Z.; Chen, X.; Hu, W.; Chuang, C.; Xie, S.; Hu, A.; Yan, W.; Kong, X.; Wu, X.; Ji, H.; et al. Cobalt in Nitrogen-Doped Graphene as Single-Atom Catalyst for High-Sulfur Content Lithium-Sulfur Batteries. *J. Am. Chem. Soc.* **2019**, *141*, 3977–3985.
51. Zhuang, R.; Yao, S.; Shen, X.; Li, T. A freestanding MoO_2-decorated carbon nanofibers interlayer for rechargeable lithium sulfur battery. *Int. J. Energy Res.* **2019**, *43*, 1111–1120.
52. Liu, Z.; Zhou, L.; Ge, Q.; Chen, R.; Ni, M.; Utetiwabo, W.; Zhang, X.; Yang, W. Atomic Iron Catalysis of Polysulfide Conversion in Lithium-Sulfur Batteries. *ACS Appl. Mater. Interfaces* **2018**, *10*, 19311–19317.
53. Kang, W.; Fan, L.; Deng, N.; Zhao, H.; Li, Q.; Naebe, M.; Yan, J.; Cheng, B. Sulfur-embedded porous carbon nanofiber composites for high stability lithium-sulfur batterie. *Chem. Eng. J.* **2018**, *333*, 185–190.
54. Li, Y.-J.; Fan, J.-M.; Zheng, M.-S.; Dong, Q.-F. A novel synergistic composite with multi-functional effects for high-performance Li–S batteries. *Energy Environ. Sci.* **2016**, *9*, 1998–2004.
55. Tang, K.; Hu, H.; Xiong, Y.; Chen, L.; Zhang, J.; Yuan, C.; Wu, M. Hydrophobization Engineering of the Air−Cathode Catalyst for Improved Oxygen Diffusion towards Efficient Zinc−Air Batteries. *Angew. Chem. Int. Ed. Engl.* **2022**, *61*, e202202671. [PubMed]
56. Guan, C.; Sumboja, A.; Zang, W.; Qian, Y.; Zhang, H.; Liu, X.; Liu, Z.; Zhao, D.; Pennycook, S.J.; Wang, J. Decorating Co/CoN_x nanoparticles in nitrogen-doped carbon nanoarrays for flexible and rechargeable zinc−air batteries. *Energy Stor. Mater.* **2019**, *16*, 243–250.
57. Cao, F.; Yang, X.; Shen, C.; Li, X.; Wang, J.; Qin, G.; Li, S.; Pang, X.; Li, G. Electrospinning synthesis of transition metal alloy nanoparticles encapsulated in nitrogen-doped carbon layers as an advanced bifunctional oxygen electrode. *J. Mater. Chem. A* **2020**, *8*, 7245–7252.
58. Peng, W.; Wang, Y.; Yang, X.; Mao, L.; Jin, J.; Yang, S.; Fu, K.; Li, G. Co_9S_8 nanoparticles embedded in multiple doped and electrospun hollow carbon nanofibers as bifunctional oxygen electrocatalysts for rechargeable zinc-air battery. *Appl. Catal. B* **2020**, *268*, 118437.
59. Bian, J.; Su, R.; Yao, Y.; Wang, J.; Zhou, J.; Li, F.; Wang, Z.L.; Sun, C. Mg Doped Perovskite $LaNiO_3$ Nanofibers as an Efficient Bifunctional Catalyst for Rechargeable Zinc–Air Batteries. *ACS Appl. Energy. Mater.* **2019**, *2*, 923–931.
60. Liu, X.; Wang, L.; Yu, P.; Tian, C.; Sun, F.; Ma, J.; Li, W.; Fu, H. A Stable Bifunctional Catalyst for Rechargeable Zinc-Air Batteries: Iron-Cobalt Nanoparticles Embedded in a Nitrogen-Doped 3D Carbon Matrix. *Angew. Chem. Int. Ed. Engl.* **2018**, *57*, 16166–16170.
61. Yang, L.; Shi, L.; Wang, D.; Lv, Y.; Cao, D. Single-atom cobalt electrocatalysts for foldable solid-state Zn-air battery. *Nano Energy* **2018**, *50*, 691–698.